A Near-Infrared Survey of NGC2024

Dylan Nelson
University of California Berkeley
dnelson@berkeley.edu

November 14, 2006

Group Members - Trey Jalbert, Donald VanNess

Abstract

We have developed a software pipeline to perform imaging, data reduction, spatial registration, and photometry on a given stellar cluster of interest. Using these tasks, we conduct a deep survey in the JHK near-infrared of the NGC2024 star-forming region using IRCAM at the Leuschner Observatory. A total of 92 sources are detected in the cluster, and 70 in the corresponding control field. Limiting magnitudes in the cluster are 12.0, 12.7, and 15.2 in Ks, H, and J, respectively. After correction for background source contamination, we use the difference between expected and observed color information to estimate an extinction of approximately 22 A_V towards NGC2024. Using a reference distance modulus of 8.1, we then present preliminary constraints on the age and mass of cluster members. Although our sensitivity limit ends up insufficient to locate brown dwarfs, we are able to make reasonable estimates of the located cluster member masses as ranging from 1.08 $M_\odot$ to 1.9 $M_\odot$, and a median age for the cluster of $2*10^6$yr.

1 Introduction

NGC2024 is an active and densely populated star-forming region[1]. For several reasons, it is an ideal candidate to conduct stellar photometry on in order to estimate interstellar extinction, distance to the cluster, and the mass and luminosity distribution of its members. Firstly, it has a large number of densely located sources. This allows the cluster to be studied with good statistical confidence, and enables the cluster to stand out clearly from the low number of background sources. Secondly, the high number density of material in the molecular clouds within NGC2024 further obscures background sources and allows for estimates of the reddening vector as well as creation of beautiful pictures.

To consider extinction, we assume that light intensity attenuates exponentially as it passes through a dusty absorbing region. The intensity I as a function of the initial intensity I_o and the optical depth τ is then given by $I = I_o e^{-\tau}$. We can re-express this change in brightness on the magnitude scale by:

$$\begin{aligned} \Delta m &= -2.5 log_{10}(I/I_0) \\ &= -2.5 log_{10}(e)\tau \\ &= 1.0857\tau \\ &= A \end{aligned}$$

Where A is the extinction. As a result, we observe that $M_\nu = m_\nu - A_\nu$ where M_ν and m_ν are the absolute and apparent magnitudes at an observed frequency ν. Interstellar extinction ratios of interest are given[2] in Table 1:

Band	λ (nm)	A/A_ν
V	551	1.000
J	1220	0.282
H	1650	0.175
K	2200	0.112

Table 1. Observational values for standard interstellar extinctions as ratios to visible extinction. Note that the wavelength dependence of extinction processes results in a decreasing amount of extinction with increasing wavelength.

We will use these values in conjunction with our derived color data in order to estimate average extinction towards NGC2024. Additionally, using a previously determined distance estimate to the cluster and our estimated extinction we will calculate the absolute magnitudes of cluster members. Finally, under the assumption that the majority of mid-range stars in NGC2024 are still on the main sequence, preliminary age and mass estimates are presented by comparing the luminosities of detected sources with main sequence spectral classifications.

2 Observations

The central NGC2024 star-forming region was surveyed from October 25-29, 2006, using the Leuschner Observatory 30-inch telescope, with the Infrared Camera (IRCAM). This camera contains a 256x256 pixel HdCdTe array, which provides a scale of 1.35" per pixel[3] for a total field of view of approximately 5.8'. Photometric observations were obtained in K' (2.2 um), H (1.65 um), and J (1.25 um) bands, imaged through their corresponding filters.

The primary data set, used throughout the remainder of this paper, was obtained on 29 October, and consisted of a 7x7 dither pattern over NGC2024 interleaved with a 7x7 dither pattern over a nearby control field[4]. An imaging pipeline was created in order to automate this process. An IDL procedure[5] *mosaic* reads from a predefined list of structures giving observing parameters for a given object: cluster and control field coordinates, dither parameters, integration times and requested bands. The *at* scheduling daemon on the Leuschner control computer is used to execute a c-shell script at the beginning of the observing night. This csh then executes individual IDL tasks and logs the output for review.

The mosaic procedure waits until the appropriate time for imaging the cluster, performs the autofocusing task, and carries out the specified imaging run. Autofocusing consists of imaging a nearby bright star through a range of secondary mirror positions. Step size in secondary position is the minimum allowed by its motor resolution, and for each position a 2D gaussian is fit to the bright star, and its FWHM calculated. To minimize fluctuations, at each position the star is imaged three times. This average FWHM varies as a function of secondary mirror position, as in Figure 1.

The minimum FWHM is retrieved and the secondary mirror reset to the optimal position. Alternatively, a "good enough" cutoff allowance is set at 2.2 pixels, such that, if we ever achieve this FWHM, the task ends and leaves the mirror in its current position. This avoids problems

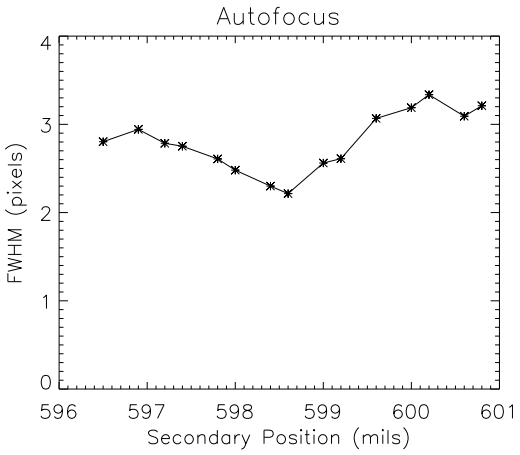

Figure 1. Output of the autofocus procedure showing the average FWHM of a 2D gaussian fit to a bright source over three exposures at each of a range of secondary mirror positions. The minima in the resultant function should represent the best focus position of the telescope.

with the resolution of the stepper motor, which makes it difficult to measure the current position accurately or return to any previously measured position exactly.

After focusing, the actual cluster is imaged. The dither offset for this observation was 0.006°, or approximately 22", resulting in a total covered area of 8.3 arcmin^2. This sequence of 49 exposures for the cluster and control field was repeated for each of the bands, where exposure time was 10 seconds for K', and 30 seconds for both H and J-bands, yielding a maximum total integration times of 8.2 and 24.5 minutes, respectively. Based on SNR considerations[6] we expect these integration times will allow detection of faint point sources approaching 15 magnitude - hopefully allowing detection of low-mass candidates as well as numerous higher mass stars necessary for statistically grounded results.

Corresponding to our observation of NGC2024, a number of standard infrared sources were also observed. The *imagestar* IDL procedure operates in the same manner as mosaic, allowing for completely automatic standard star imaging. For a requested star in its structure database, it will wait until the appropriate time for imaging, point and set appropriate filters on the telescope, perform autofocusing on a nearby bright source, and image the standard star in a given NxN raster pattern. It is launched before or after observations of a stellar cluster. The results can be used to place magnitudes on an absolute scale.

3 Data Reduction

Individual exposures were corrected for systematic errors, and were then spatially registered in order to form a single mosaic for each band. Each band mosaic was then aligned to create a false-color image. This image cube was then the basis for source location and photometric calculations.

3.1 Error and Bias Considerations

Previously developed techniques to calibrate the data were applied to individual exposures as the first step in processing. An average sky-subtraction frame was calculated as the median through the cube of control field images. Where possible, highest and lowest pixel values were dropped in this median in order to eliminate contribution from stars and cosmic rays. The cluster images were then sky-subtracted by this median frame. Due to the time-variability of the sky brightness, however, a gradient of sky background was visible from one science frame to the next. A scalar background offset was calculated, as the difference between the corresponding control frame median and the master control frame median, for each cluster frame, eliminating this sky gradient.

Twenty-five flat field exposures were taken for each band at sunrise twilight the day following our science observations. Darkframes were taken corresponding to the flat exposure times. A weighted master flatfield was then created from each 5x5 raster pattern, where weighting was inversely proportional to standard deviation of the individual frames. Pixels in this master flat exhibiting deviation greater than 5σ from the mean were flagged to a large value. Additionally, a cut-off at 20% above and below the median of 1 was enforced. By flagging to a large value, division by the modified flat effectively reduces bad pixel values in the final image to zero.

3.2 Multi-Frame Mosaic

An IDL procedure *merge* was created which requires as inputs only the same object and epoch structures created for the actual imaging process. It dynamically creates registered three-dimensional cubes for both the cluster and control fields, ready for analysis in a photometry

package. The actual steps in this process are described below.

We first load all the individual exposures and apply the previously described data calibration steps. Next, the frame closest to the center of our dither pattern is selected as a reference frame, r. For every frame, f_i, the cross-correlation is then computed as[7]:

$$c(x) = r \star f_i = \int_{-\infty}^{\infty} r(u-x) f_i(u) du \quad (1)$$

The resultant $c(x)$ is a matrix, each entry corresponding to a certain lag. The maximum of this matrix is then located. The amount of "lag", or shift in both x and y, corresponding to this maxima results in the highest correlation between the i^{th} frame and the reference frame. A 2D gaussian profile is fit to the vicinity of this point in order to calculate non-integer shifts. A fractional shift was implemented with linear interpolation between pixels, but it resulted in a loss of apparent focus of point sources, and was discarded in favor of simple integer shifts. If Δx_i and Δy_i represent the x and y shifts of the i^{th} frame, then the dimensions of the final array are calculated as:

$$X = max(|\Delta x|) + max(\Delta x + X_{ref}) \quad (2)$$
$$Y = max(|\Delta y|) + max(\Delta y + Y_{ref}) \quad (3)$$

Where X_{ref} and Y_{ref} are the x and y dimensions of the reference frame. Each frame is placed in a new array of this size and shifted to its appropriate position. A corresponding exposure map is created, where each pixel in the exposure map gives the amount of exposure time of that pixel in the final mosaic. A representative exposure map is shown in Figure 2.

As with the flat field, zeros in the exposure map are flagged to a large number prior to division to prevent infinities. The final mosaic for each band is divided by this exposure map, thereby normalizing all values to counts per second.

We now have three mosaic images of the cluster corresponding to each of the three observational bands. These can be spatially registered and assigned as three layers in a 3D data cube by following an identical procedure to the above. Repeating the process once more for the control field data yields a second control data cube. The fully registered cluster cube is shown unaltered in 24-bit color in Figure 3, where K, H, and J bands correspond to red, green, and blue (RGB) color channels, respectively.

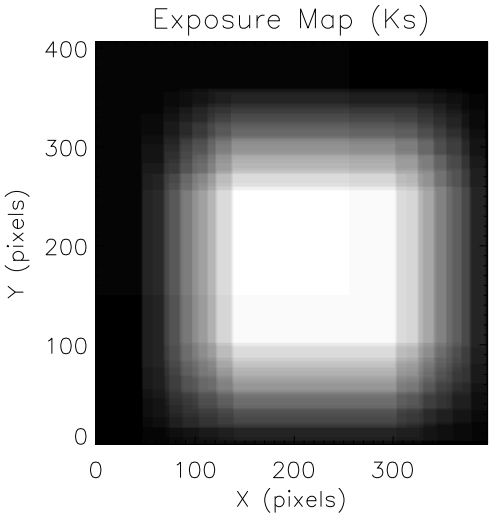

Figure 2. A representative exposure map, this shows the exposure time for each pixel in the Kshort-band mosaic of NGC2024. The center has maximum combined integration time of 490 s, and the outer edges have zero exposure time.

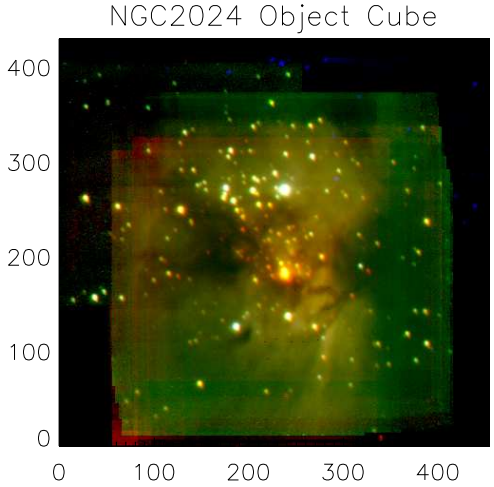

Figure 3. An unedited full view of the data cube for NGC2024. The unrestricted field of view is approximately 8.3'. The intensity scale is linear, bounded from zero to 100 counts per second.

A cropped and post-processed "pretty" image is shown in Figure 4:

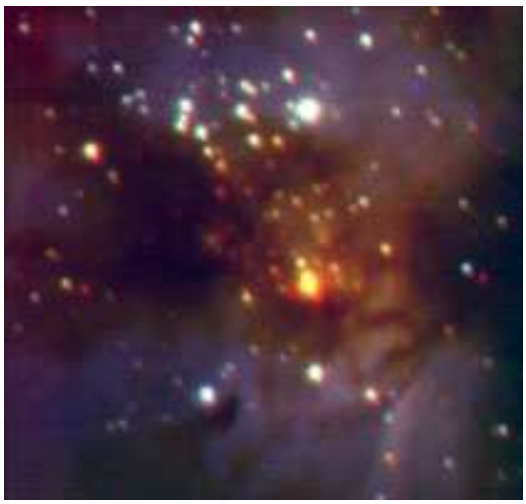

Figure 4. A cropped image of NGC2024, corresponding to a field of view of approximately 6'. The region shown represents good SNR coverage in all three bands. This image is displayed with a logarithmic intensity scale, with pixel values truncated from 2.5_{10} to 60_{10}.

3.3 Astrometry

Point source location, or astrometry, is performed with an identical procedure for the cluster and control cubes. A reference band is chosen, and source identification is carried out on that band. Since the three band mosaics are already registered, we are guaranteed that identical sources occur at the same (x,y) positions in the other band mosaics. Several methods were considered in order to perform astrometry. First, the *slocate*[8] procedure was run on the reference band image itself. However, NGC2024 contains extended clouds of dust and gas which are back-illuminated and thus can be extremely bright. Due to false positives and an inability to locate extremely faint sources, this technique was discarded.

Ideally, we would like to use a convolution based solution. The two-dimensional convolution $c(x, y)$ of an image $f_i(x, y)$ by a given convolution kernel $k(x, y)$ is given[9] by Equation 4:

$$c(x,y) = f_i(x,y) \star\star k(x,y) = \int_{-\infty}^{\infty}\int_{-\infty}^{\infty} f_i(x',y')k(x-x',y-y')dx'dy'$$

The optimal kernel for source location would be a gaussian identical to the PSF of the observing telescope. Using slocate to locate highly probable sources in the original images, fitting 2D gaussian profiles and calculating the FWHMs, we create a crude model of the PSF and convolve the reference band mosaic with this kernel. Although source detection is both complete and accurate, it does not always find the same sources as the kernel used for convolution-based photometry, as described in the next section. Thus, in order to eliminate inconsistencies, our "photometry kernel" was also used as a source detection kernel. Figure 5 shows a grayscale H-band mosaic image of NGC2024 with overlaid circles on located sources.

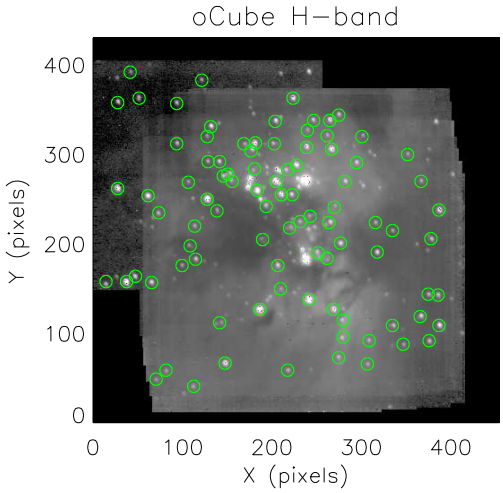

Figure 5. H-band mosaic of NGC2024, scaled logarithmically from 2.5 to 60 counts per second. Identified sources from our astrometry procedure are overlaid with green circles. In this image 92 sources were used, with magnitudes ranging from 7.1 to 12.7.

Note that false positives did occur, especially when searching for sources of fainter and fainter luminosity. As a result, an ordered exclusion list was created to identify bad locations and exclude them from further analysis. This exclusion process is separate from consideration of contamination from stars not in the cluster, which occur in three forms: (1) foreground sources, (2) spatially local though unrelated sources, and (3) background sources. These sources of confusion are considered further in Section 4.1.

3.4 Photometry

The convolution kernel was a two-dimensional array constructed from the sum of a positive circular mask and a negative annulus mask. The height of the positive circle was left at unity. The

effect of this circular mask is then to sum the contribution of all the pixels within it. The height of the negative annulus, H_a, was normalized as in Equation 4:

$$H_a = \frac{N_c}{N_a} \quad (4)$$

Where N_c and N_a are the number of pixels in the circle and annulus, respectively. This normalization insures that the total of the kernel is zero. As a result, the kernel multiplied by any region of uniformly empty sky returns zero, and when multiplied by a region containing a source of known intensity returns exactly that intensity minus the vicinity sky background value. In order to optimize SNR and avoid contamination of measurements due to the high surface density of sources in the field the circle radius and annulus inner and outer radii were chosen as 4, 5, and 8 pixels, respectively. In order to increase certainty in our results a number of slightly different kernels were tested, and the photometric results confirmed independent of reasonable variation of these parameters. The actual kernel used is shown in 2D in Figure 6.

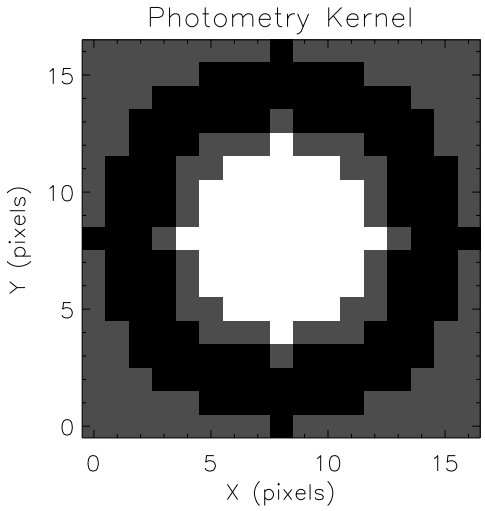

Figure 6. The photometric convolution kernel visualized in 2D. The white central circle has value unity, the black annulus has value as previously discussed, and the grey regions represent zero value. As a result, the total of pixel values for this kernel is zero.

Each band mosaic was convolved with this kernel. The local maxima about the previously determined source locations is extracted and saved. The resulting values are counts per second, $N_\star/t_\star$, which can be converted to apparent magnitudes by the expression in Equation 5:

$$m_\nu^\star = m_\circ - 2.5log_{10}\left(\frac{N_\star}{t_\star}\right) + 2.5log_{10}\left(\frac{N_\circ}{t_\circ}\right) \quad (5)$$

Where $N_\circ/t_\circ$ and $m_\circ$ are the counts per second and magnitude of our observed standard star. To place our photometric measurements on an absolute scale measurements of infrared standard stars[10] HD201941 and HD203856 were used.

4 Results and Discussion

Having apparent magnitudes in Ks, H, and J bands for all of our detected sources in both the cluster and control fields, several informative diagrams can be constructed. Before proceeding, though, we would like to confirm that our cluster region shows a statistically significant excess of sources as compared with a control field of background galactic contamination. The Kolmogorov-Smirnov test determines if two data sets are drawn from the same parent population. The K-S statistic is defined[11] simply as the maximum value of the absolute difference between two distribution functions. We conducted the K-S test on all three bands and found a negligibly nonzero probability that they were drawn from the same parent population. That is, the cluster image exhibited a clear statistical excess of sources as compared with the control field. Before proceeding further, however, we still need to estimate and correct for the level of background contribution.

4.1 Luminosity Function

First, we recognize the contribution of background sources contaminating our primary region of interest. We expect that the small spatial extent of NGC2024, combined with its high density molecular cloud, will obscure the majority of background stars and insure those we do detect are within the cluster itself. However, to get a measure of this error, photometry was also performed at a similar galactic latitude (b=-17° for NGC2024) on a nearby control field. The magnitude distributions in Ks, H, and J-bands are given in Figures 7, 8 and 9, respectively. In each case the detected cluster sources are given as histograms shaded diagonally down and to the right, while detected control field sources are overplotted with a cross-hatch shading.

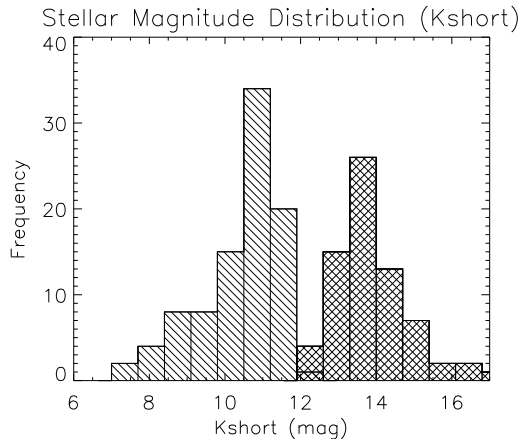

Figure 7. The magnitude distribution for detected stars in the Ks-band. Source magnitudes in the cluster range from magnitude 7.3 to 12.0, and in the control field from 12.0 to 17.1.

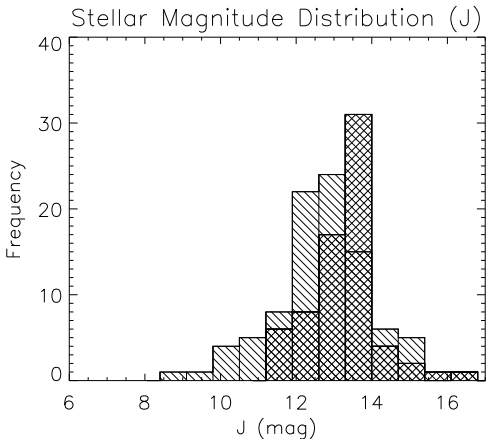

Figure 9. The magnitude distribution for detected stars in the J-band. Source magnitudes in the cluster range from magnitude 8.7 to 16.7, and in the control field from 11.4 to 16.2.

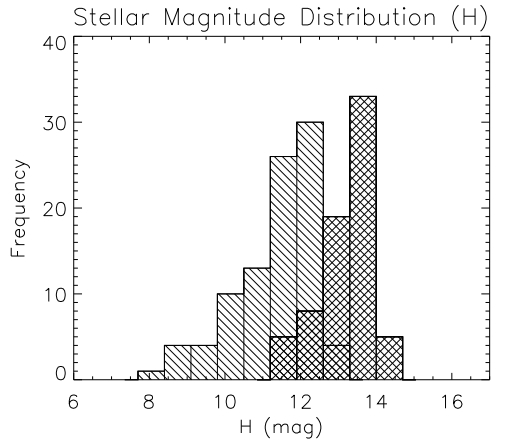

Figure 8. The magnitude distribution for detected stars in the J-band. Source magnitudes in the cluster range from magnitude 8.3 to 12.7, and in the control field from 11.3 to 14.1.

H and J distributions exhibit an expected overlap between the cluster and control fields. In both cases the majority of sources detected in the control field had m $\geq$ 12, with significant populations occurring at m = 14 and greater. We conclude that up to this magnitude the detected sources in our cluster are indeed within NGC2024, and are not due to background contamination. At m = 14 and greater, however, source detection levels in the cluster and control fields are similar. As a result, we cannot definitively conclude that any detected cluster sources at this magnitude are indeed within NGC2024, as opposed to in the background of our field of view.

The Ks-band data exhibits several undesirable characteristics. Since the limiting magnitude for the cluster is approximately 12.0, we do not see the peak of $m_K \simeq 12$, as expected[12]. That is, our survey is complete at best only to $m_K \simeq 11$. Furthermore, the observation of the control field at Ks exhibited extremely poor characteristics, including both total signal and SNR. Although this occurred for as of yet unknown reasons, it resulted in the shift of the control distribution to fainter magnitudes than realistically exist.

Despite this erroneous behavior at the Ks-band, we could construct a cluster luminosity function by preforming bin-by-bin subtraction of the two histograms for, e.g., H-band. The resulting histogram would represent the stellar magnitude distribution corrected for contamination by unrelated stars. We omit this step in favor of overplotting the two distributions on the same graph, as above.

4.2 Color and Infrared Excess

Having confidence that the stars in our survey are actually contained within the stellar cluster of interest, we can make the assumption that they reside within a spatially concentrated region, which is at all points equidistant from us. As a result, the differing apparent intensities as a function of wavelength can be visualized within a color-magnitude diagram as well as a color-color diagram. The color-magnitude diagrams of the cluster and control field, respectively, are shown

in Figures 10 and 11.

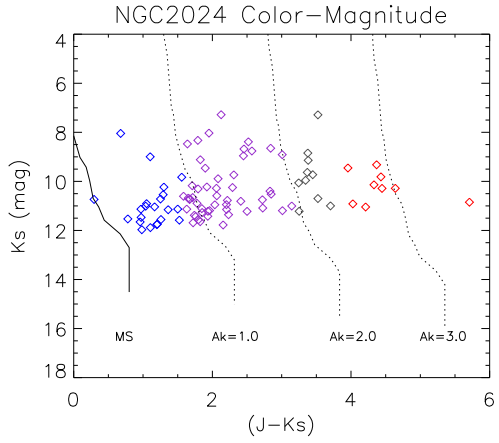

Figure 10. Color-magnitude diagram of the stellar cluster. The solid line represents the main sequence at a distance equal to that of NGC2024, 415pc. The dotted lines represent that same predicted main sequence experience variable levels of K-band extinction, as labeled. Data point colors are as in Figure 12.

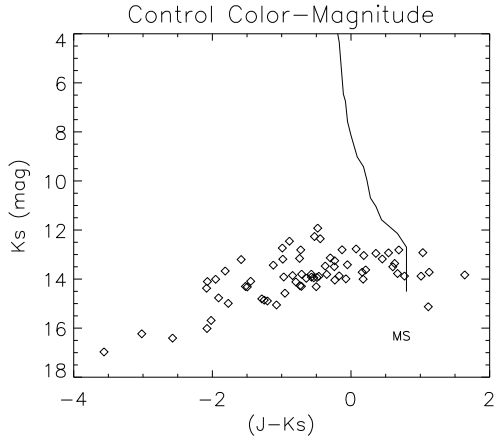

Figure 11. Color-magnitude diagram of the control field. As above, the solid line represents the main sequence at an equivalent distance modulus of NGC2024. We observe a broad distribution of stars with negative (J-Ks) values, thought to be due to the bad K-band control field data.

The color-magnitude diagram for the cluster exhibits significant reddening away from the main sequence, while we expect the control field stars to have no association and no locally intervening ISM, and thus to fall much more closely on the main sequence line. Due to bad Ks-band data in the control, however, its color-magnitude diagram appears more spread out in (J-Ks) color than expected.

The overplotted extinction lines give a rough estimate of extinction towards cluster members. We can see that stars in NGC2024 consistently experience extinction in K ranging from zero to 3 magnitudes, with one outlier at approximately A_K=4.0. From Table 1 we see that this corresponds to a maximum visible extinction of A_V=26.8 magnitudes. Alternatively, we observe from Table 1 that

$$A_J - A_K = (0.282 - 0.112)A_V = 0.l7A_V.$$

Such that extinction in the visible band is given by Equation 6:

$$A_V = \frac{\Delta\left(A_J - A_K\right)}{0.17} \tag{6}$$

From Figure 10 we measure a maximum $\Delta\left(A_J - A_K\right) \simeq 5$ mag, corresponding to a maximum A_V of 29 magnitudes. As a check, we expect the visible extinction to follow[13] Equation 7:

$$A_V = \frac{N_H}{(1.79 \pm 0.03) * 10^{21} cm^{-2}} \tag{7}$$

Where N_H is the column number density of hydrogen in the line of sight. Our value for A_V requires $N_H \simeq 5.2 * 10^{22} cm^{-2}$, which is not unreasonable for an extremely dense H II star-forming region such as NGC2024.

As an alternative to converting main sequence predictions to a given distance modulus, we can evaluate relative colors only. The color-color diagrams of the cluster and control field are given in Figures 12 and 13.

The interstellar reddening vectors in both the color-color diagrams are calculated as having a slope m given by Equation 8:

$$m = \frac{A_J/A_V - A_H/A_V}{A_H/A_V - A_K/A_V} \tag{8}$$

Where m follows the axes of the color-color diagram, and stars within the two reddening bands represent expected interstellar extinction. Stars outside this region therefore represent infrared excess stars. Proportions of normal vs infrared excess stars contain information about young stellar evolution in environments similar to that of NGC2024. This includes the existence of circumstellar disks/protodisks, collapsing mass clouds forming new stars, and other phenomena leading to unexpected infrared emission. A deeper survey of NGC2024 could tackle

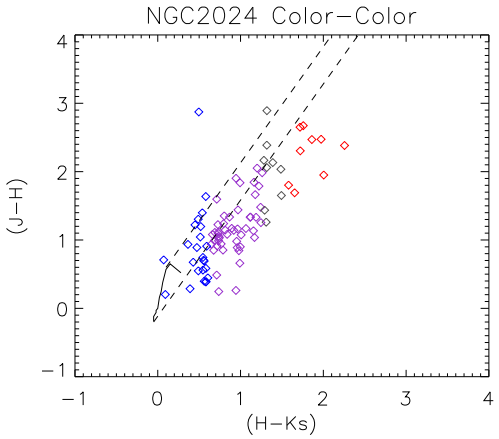

Figure 12. (J-H) vs (H-Ks) color-color diagram for NGC2024. The solid line represents the main sequence, and the dashed lines are reddening lines. Symbol color is a linear function of (H-Ks) from blue to red. We observe the significant number of sources lying outside the main sequence reddening lines.

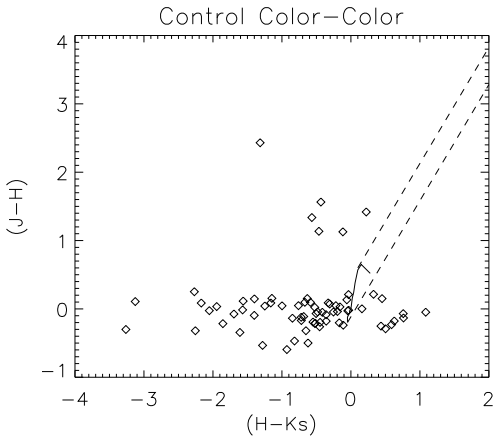

Figure 13. The identical (J-H) vs (H-Ks) color-color diagram for the control field. The solid line represents the main sequence, and dashed lines are reddening lines. The poor quality of the selected control field leads to undesired results, including large negative (H-Ks) values.

such questions with data and techniques similar to those presented here.

The (J-H) versus (H-Ks) distribution of the cluster appears as expected. A number of sources fall near the main sequence, shown as a solid line, and a large portion fall within the reddening lines, overplotted as two dashed lines. A large portion also falls to the right of these sources, though, representing stars experiencing larger (H-Ks) colors than theoretically predicted - extinction. The color-color diagram of the control field is less informative, as it suffers from the same defects as the color-magnitude diagram. The fact that stars fall to the left of the main sequence line is a strong indicator of faulty data. Specifically, a disproportionately low weighting of the Ks band with respect to H and J. Despite this, we still have enough information to make preliminary estimates of quantities which are not directly observable, but rather can be derived from our above color and luminosity function results.

4.3 Mass and Age Constraints

Taking the distance to NGC2024 as a given, we can effect a conversion from apparent to absolute magnitudes by using our above estimates for interstellar extinction. For a distance d in parsecs and an apparent magnitude m, the absolute magnitude M is given by Equation 9:

$$m - M = 5log_{10}\left(\frac{d}{10pc}\right) + A_\nu \qquad (9)$$

Where A_ν is the extinction. Using a distance $d = 415pc$[14], we convert our magnitudes from an apparent to absolute scale. The resulting minimum, maximum, and mean absolute magnitudes for each of JHK bands is given in Table 2:

Band	M_{min}	M_{max}	$\bar{M}$
J	3.42	-4.41	-0.47
H	1.48	-2.98	0.14
K	1.87	-2.81	0.31

Table 2. Absolute magnitude calculations for each of the JHK bands. K band extinction is set at 2.0 magnitudes, and the others follow as given in Table 1. Minimum, maximum and mean magnitudes are given.

From this table we conclude that the fainest star spectral types in K, H, and J bands, respectively, are F0, A5, and G0. Ages of these objects could theoretically be calculated from main sequence spectral classification, but would provide only a range of lower bounds on the age. The corresponding masses[15] are 1.6, 1.9, and 1.08 times the solar mass. These are certainly reasonable estimates of medium to low mass stellar objects, though clearly we have not located any brown dwarf candidates with masses of $\simeq 0.3\ M_\odot$. With our limiting magnitude of 12.7 in H-band, however, we would not expect to have the sensitivity to locate brown dwarfs. A second observational epoch was planned with a 13x13 raster

pattern with offset steps of 0.03 degrees, which would have resulted in nearly twice the total integration time for the central regions. However, weather and time constraints prevented these observations.

Finally, a more advanced alternative to determining the age of the cluster would involve a dereddening procedure utilizing isochrone fitting techniques[16], which is too complex for the purposes of this paper. Rather, we qualitatively compare our apparent K magnitude luminosity function to the model from Lada & Lada, 1995. Their model assumes a distance modules of 7.5, and is normalized to 1000 stars. Based on best shape considerations, as well as the peak and falloff points of the model, our data for NGC2024 appears to coincide with a lower age limit of $2*10^6$yr, to an error of approximately $\pm 1*10^6$yr. This value is in good agreement other literature[17] involving near-infrared imaging of NGC2024.

5 Conclusions

We have successfully imaged NGC2024 at the Ks, H, and J bands in order to construct a semi-deep infrared survey image. After tailoring a point source location task to preform astrometry, convolution-based photometry was carried out across all three bands for both the cluster and a nearby control field. Despite data integrity issues in the Ks observations of the control field, the magnitude distribution functions were determined statistically relevant as per the K-S test. Contamination corrected luminosity functions provide the limiting magnitudes of our observations at each band, as well as the ability to estimate the completeness of our survey at a given magnitude. Furthermore, they relate directly to underlying properties of young stellar populations such as the mass function.

Color-magnitude and color-color diagrams provide a viable route to estimating interstellar extinction towards NGC2024, and correction for this extinction - combined with a known distance to the cluster - enables absolute magnitude calculations as well as main sequence classification for our detected sources. From this we estimated the mass and age of the lowest luminosity sources, in hopes of finding possible brown dwarf candidates. In this case our limiting magnitude was unable to detect these faint objects, however calculation shows that a slightly deeper integration run would enable detection of these and other faint objects of interest with our developed data reduction and analysis techniques. The ability for interesting and novel science from such observations is shown in the literature as short ago as 10 to 15 years. Imaging in the near-infrared, then, offers an accessible and viable technique for investigating the nature of, and science behind, young star-forming regions such as NGC2024.

References

[1]SIMBAD coordinates for NGC2024 are given as α=05°44'41", δ=-01°54'17" (J2000.0)

[2]Graham: "Imaging an Obscured Star Cluster" p8.

[3]Graham, J.R., Treffers, R. R.: "An Infrared Camera for Leuschner Observatory"

[4]A suitable control field was chosen at α=06°10'00", δ=-01°15'17" (J2000.0), which added a 50 second overhead per exposure due to the interleaving process.

[5]See http://ugastro.berkeley.edu/∼dnelson/ for source code of all IDL tasks used.

[6]See Nelson, D.: "Stellar Photometry" for a required integration vs. achievable SNR plot.

[7]Bracewell, R.N.: "The Fourier Transform and Its Applications" p46. Note we actually use the discrete form of this integral representation.

[8]See Nelson, D.: "Stellar Photometry" for a description of the slocate routine.

[9]Bracewell, R.N.: "The Fourier Transform and Its Applications" p243.

[10]See Elias et al.: "Infrared Standard Stars".

[11]Press et al., 1992: "Numerical Recipes".

[12]Lada et al., 1991b, Hodapp, 1994, and Comeron, Rieke and Rieke, 1996 all observed such a characteristic.

[13]Predehl and Schmitt, 1995.

[14]Equivalent to a distance modulus of 8.1, Anthony-Twarog, 1982.

[15]Carroll and Ostlie: "Modern Astrophysics"

[16]See details in Strom et al., 1993, or D'Antona & Mazzitelli, 1995.

[17]See for example Comeron, Rieke & Rieke, 1996: "Properties of Low-Mass Objects in NGC 2024".